Flow past triangular airfoil of variable thickness with low Reynolds number in Mars atmosphere

Kumar, Ankit

Flow past triangular airfoil of variable thickness with low Reynolds number in Mars atmosphere

Wen-Chung Wu & Ankit Kumar

Published online: 16 May 2024.

Submit your article to this journal ↗

View related articles ↗

View Crossmark data ↗

Taylor & Francis
Taylor & Francis Group

Check for updates

Flow past triangular airfoil of variable thickness with low Reynolds number in Mars atmosphere

Wen-Chung Wu (iD) and Ankit Kumar (iD)

Department of Aeronautical Engineering, National Formosa University, Yunlin, Taiwan

ABSTRACT

Aerodynamic research on Mars for the past few decades has increased in the development of optimum aerial vehicles for Mars. The current research aims to study the aerodynamics of a triangular airfoil in Mars atmospheric conditions and understand the future regions of flow improvement. A numerical investigation using a Finite Volume Solver has been performed for $0°$ to $16°$ angles of attack at low and high flow velocities. Low flow velocities ranging from Re = 3,000 to 7,000 have been considered for the investigation. The nonlinearity in C_l appears as the separation bubble begins to approach the apex on the suction surface. Apart from the separation bubble, a flow recirculation zone is generated for low and high Re. at $\alpha = 16°$. The highest aerodynamic performance is at $\alpha = 6°$.

1. Introduction

Mars, one of the most extensively studied planetary bodies in the solar system, has garnered significant attention from researchers due to its potential for habitability. Numerous missions have been launched to explore its atmosphere, geology, and other aspects. Compared to Earth, Mars has a much thinner atmosphere, with a surface pressure of less than 1% of Earth's atmospheric pressure. This low pressure significantly impacts the aerodynamics of aircraft, as well as other factors such as propulsion and thermal management. The low-density atmosphere of Mars presents challenges for designing aircraft that can generate enough lift to stay airborne.

In general, aircraft on Mars will need to fly at much lower speeds and use larger wing areas than on Earth to achieve the same level of lift. The low atmospheric density also means that the airfoils of Mars aircraft need to be specially designed to operate in compressible, low Reynolds number flow. The low Reynolds number flow regime encountered in the Martian atmosphere necessitates the use of specialized airfoils, as conventional airfoils would not be effective. Furthermore, the low gravity of Mars, which is only about 37% of Earth's surface gravity, affects the weight forces experienced by aircraft. This can be both an advantage and a disadvantage in aircraft design. On the one hand, the lower gravity means that aircraft can be designed to be much lighter and more fuel-efficient than on Earth.

Several studies have been conducted to investigate the aerodynamics of Martian entry, descent, and landing systems using computational fluid dynamics (CFD) simulations. Jiang et al., [1] investigated how geometric porosity affects the flow patterns and aerodynamic properties of the SSDS parachute derivative model in a supersonic setting. In another study to analyze the characteristics of the Mars helicopter's flight dynamics in hovering and forward flight more effectively,

---

CONTACT Wen-Chung Wu ✉ wuwenj@nfu.edu.tw 📄 Department of Aeronautical Engineering, National Formosa University, Yunlin, Taiwan

a rotor aerodynamic surrogate model is constructed and used by Zhao et al., [2]. Over the entire Martian surface, Hebrard et al., [3] have created a map of the aerodynamic roughness length. Instead of extrapolating from the sparse ground truth data to infer a "idealized" coverage of this parameter, the authors have opted to use rock abundance data sets to create a high-resolution mapping of this parameter.

Furthermore, experimental studies have also been conducted to study the aerodynamics of Martian entry, descent, and landing systems. Direct simulation and free-molecular Monte Carlo codes are used by Moss et al., [4] to calculate the aerodynamics. The calculations reveal that Pathfinder exhibits statically unstable behavior throughout much of the rarefied transition regime. In another study, Edquist et al., [5] have tried to provide an overview of the predicted Phoenix entry capsule aerodynamics for use in six-degree-of-freedom trajectory pre- and post-flight analyses. The aerodynamics database has been developed with similar methodology that uas used for MER and Pathfinder databases, with modifications tailored for Phoenix entry trajectory. The most recent Mars investigation included a co-axial helicopter by Balaram et al., [6] although land-based vehicles have been sent to investigate the planet, an aerial vehicle makes the investigation much easier. Koning et al., [7] has developed a rotor model focusing on aerodynamics for Mars helicopters. Kumar [8] have performed aerodynamic simulation using Spalart-Allmaras turbulence model for S1223 airfoil for low and high Re and triangular airfoil in [9].

The triangular airfoil has been investigated for low Re = 3,000, 4,000, 5,000, 6,000, and 7,000. The maximum thickness of the airfoil has been changed Δh being 0.04C, 0.045C, 0.05C, and 0.06C. The current research aims to see if the earlier investigated airfoils are best to study aerodynamics of the airfoil or there could be a better understanding of aerodynamics if the design is changed.

2. Research methodology

2.1. Governing equations

Flow over an airfoil is governed by the Navier-Stokes equation, neglecting the source terms.

$$\frac{\partial \rho}{\partial t} + \frac{\partial(\rho u)}{\partial x} + \frac{\partial(\rho v)}{\partial y} = 0 \tag{1}$$

$$\frac{\partial(\rho u)}{\partial t} + \frac{\partial(\rho u^2)}{\partial x} + \frac{\partial(\rho uv)}{\partial y} = -\frac{\partial P}{\partial x} + \frac{\partial}{\partial x}\left(-\frac{2}{3}\mu\left[\frac{\partial u}{\partial x} + \frac{\partial v}{\partial y}\right] + 2\mu\frac{\partial u}{\partial x}\right) + \frac{\partial}{\partial y}\left(\mu\left[\frac{\partial v}{\partial x} + \frac{du}{\partial y}\right]\right) \tag{2}$$

$$\frac{\partial(\rho v)}{\partial t} + \frac{\partial(\rho u v)}{\partial x} + \frac{\partial(\rho v^2)}{\partial y} = -\frac{\partial P}{\partial x} + \frac{\partial}{\partial y}\left(-\frac{2}{3}\mu\left[\frac{\partial u}{\partial x} + \frac{\partial v}{\partial y}\right] + 2\mu\frac{\partial v}{\partial y}\right) + \frac{\partial}{\partial x}\left(\mu\left[\frac{\partial u}{\partial y} + \frac{dv}{\partial x}\right]\right) \quad (3)$$

Equations (1), (2), and (3) represent mass and momentum conservation in the x and y directions. Where μ is the kinematic viscosity, u is the velocity of the fluid parcel; p is the pressure, and ρ is the density of the fluid.

While solving the Navier-Stokes equations with Reynolds-Averaged Navier-Stokes (RANS) turbulence modeling is a common approach, Unsteady-RANS has been chosen for this research due to limited knowledge of flow behavior in the Martian atmosphere, as evidenced by a dearth of literature. URANS balances computational efficiency and accuracy by considering unsteady effects, providing a more comprehensive understanding of flow phenomena without the computational demands of fully resolved simulations like LES, DES, or DNS.

The Spalart-Allmaras (SA) turbulence model is well-suited for low Reynolds number flows. Spalart and Allmaras [10] developed a one-equation turbulence model for aerodynamic flows widely used in CFD simulations. The accuracy of the SA model in simulating low Reynolds number flows due to its ability to account for the effects of turbulence on the eddy viscosity, which is particularly useful in modeling the thin boundary layer of the Mars atmosphere. Ning and Xu [11] used the Spalart-Allmaras model equation after converting it to conservative form for investigating the transonic compressor rotor flow highlighting the model's effectiveness in predicting heat transfer in complex flow geometries with both external and internal flows. Liu et al., [12] assessed turbulence models for low Reynolds number flows over airfoils.

The SA model uses a transport equation for a turbulent viscosity-like quantity, known as the turbulence kinetic energy (k) and its dissipation rate (ω). The model solves for the eddy viscosity through a relationship between k and the turbulent length scale. The model has been shown to be effective in predicting turbulent flow characteristics in various aerodynamic simulations. The SA model [13] is particularly effective for low Reynolds number flows where other models may struggle due to their complexity.

$$\frac{\partial}{\partial t}(\rho\tilde{v}) + \frac{\partial}{dx_i}(\rho\tilde{v}u_i) = G_v + \frac{1}{\sigma_{\tilde{v}}}\left[\frac{\partial}{\partial x_j}\left\{(\mu + \rho\tilde{v})\frac{\partial\tilde{v}}{\partial x_j}\right\} + C_{b2\rho}\left(\frac{\partial\tilde{v}}{\partial x_j}\right)^2\right] - Y_v + S_{\tilde{v}} \quad (4)$$

Where G_v is the production of turbulent viscosity, and Y_v is the destruction of turbulent viscosity that occurs in the near-wall region due to wall blocking and viscous damping. $\sigma_{\tilde{v}}$ and C_{b2} are the constants, and v is the molecular kinematic viscosity. $S_{\tilde{v}}$ is a user-defined source term.

At low Knudsen numbers (Kn < 0.01), molecular effects are negligible [14, 15], allowing the accurate representation of flow using the Navier-Stokes equations. The continuum assumption applies to flows where the relevant Knudsen number is approximately below 0.01. In these cases, molecular effects predominate.

$$\lambda = \frac{BT}{\sqrt{2}\pi d^2 p} \quad (5)$$

$$\lambda = \frac{1,381 \times 10^{-23} \times 248.2}{1.414 \times 3.14 \times (3.3 \times 10^{-10})^2 \times 703.10} = 1.0082 \times 10^{-5}$$

$$L = C = 1$$

$$Kn = \frac{\lambda}{L} = 1.0082 \times 10^{-5}$$

2.2. Computational domain and meshing

In CFD simulations, a mesh is a discretized representation of the computational domain. It is required to depict the geometry properly, make numerical solutions to the governing equations easier, ensure conservation principles, establish boundary conditions, examine grid independence, and achieve computing efficiency. A well-designed mesh is critical for producing trustworthy and accurate results in CFD simulations. The mesh represents the physical geometry of the issue numerically. It divides the domain into a finite number of cells, allowing partial differential equations that describe fluid flow or heat transfer processes to be solved.

Figure 1 and 2 shows the computational domain and the grid, respectively. The domain has been developed with boundaries very far from the airfoil to ensure they would not affect the flow behavior. C is the chord length, Δh is the maximum thickness of the airfoil at 0.3C distance from the leading edge. For the current research, only Δh has been varied. The mesh has been generated for simulating the atmospheric fluid flow in Martian conditions. A fine grid has been made near the airfoil surface, whereas coarse mesh has been generated at other regions comparatively [9].

2.3. Boundary conditions

According to Versteeg [16], boundary conditions are crucial to computational fluid dynamics (CFD) simulations. For low Reynolds number flows, boundary conditions are velocity inlet to define inlet flow velocity and pressure outlet to specify the static pressure at the outlet, alongside wall conditions, commonly enforcing no-slip assumptions to airfoil.

In ANSYS Fluent, the convergence criteria are based on residual values. A residual level of 10^{-6} is frequently regarded as an adequate convergence threshold for many aerodynamic models.
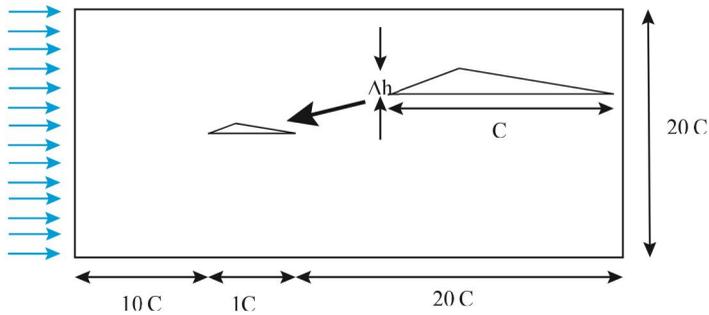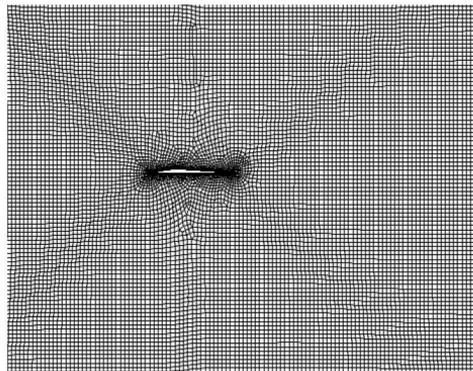

Figure 1. Computational domain.

Figure 2. Computational mesh.

Table 1. Grid independence study.

Mesh	No. of Elements	Cl	Cd
1	172,477	0.1341	0.0571
2*	249,577	0.1228	0.0621
3	389,160	0.1159	0.0614
4	481,862	0.1189	0.0599
Caros (DNS) [17]		0.121	0.06

Table 2. MC1 Operating conditions [7].

Variables	Values	Variables	Values
Atmospheric Composition	$> 95.00 \% \ CO_2$	g	3.71 m/s^2
Density	0.015 kg/m^3	Pressure	703 Pa
Operating Temperature	248.20 K	Sound speed c_s	245.835 m/s
Dynamic Viscosity	$1.13 \times 10^{-5} \ Ns/m\hat{2}$	Gas constant (CO_2)	188.9 J/kg K
Specific Heat Ratio	1.289		

The time step size of 0.0004s has been computed for the unsteady simulations, fulfilling the Courant-Friedrichs-Lewy (CFL), regarded as one of the numerical stability criteria. Transient simulations have been performed, and all the simulations have been calculated up to 40 s of flow time.

2.4. Grid independence study

To perform a grid independence study, a simulation is run using a sequence of increasingly finer grids, starting from a coarse grid and gradually increasing the resolution until the solution converges to a desired level of accuracy. A comparison of the solutions obtained from the various grids is then conducted to ascertain the sensitivity of the solution to grid resolution and to determine the optimal grid size for the given simulation. Table 1 shows the table of various mesh developed and investigated for Re. 3,000 at $\alpha = 0°$. Although no major differences have been found when meshes 2, 3, and 4 are simulated, the values in the present research are closest to existing literature when the second mesh having 249,577 elements has been investigated [9]. As our results agree with that of Caros [17], a second mesh has been used for future numerical simulations in the research.

2.5 Mars atmospheric conditions

The Martian atmosphere mainly comprises carbon dioxide (CO_2) with small amounts of nitrogen and argon. It also has traces of water vapor and methane. The thin Martian atmosphere also affects the way sound travels on the planet. Sound waves on Mars have a much lower frequency and travel much slower than Earth. However, the Martian atmosphere is much thinner than Earth's, so sound waves travel much slower and have a lower frequency. The atmospheric conditions of Mars have been used in the current research from research by Koning [7] from Martian Conditions (MC1), as shown in Table 2.

2.6 Code validation

Flow around the triangular airfoil in Martian atmospheric conditions has been done at Reynolds number 3,000, and the aerodynamic force coefficients have been compared with the existing literature of numerical and experimental results [9]. Figure 3 shows the graphs for validating our results from the existing literature.
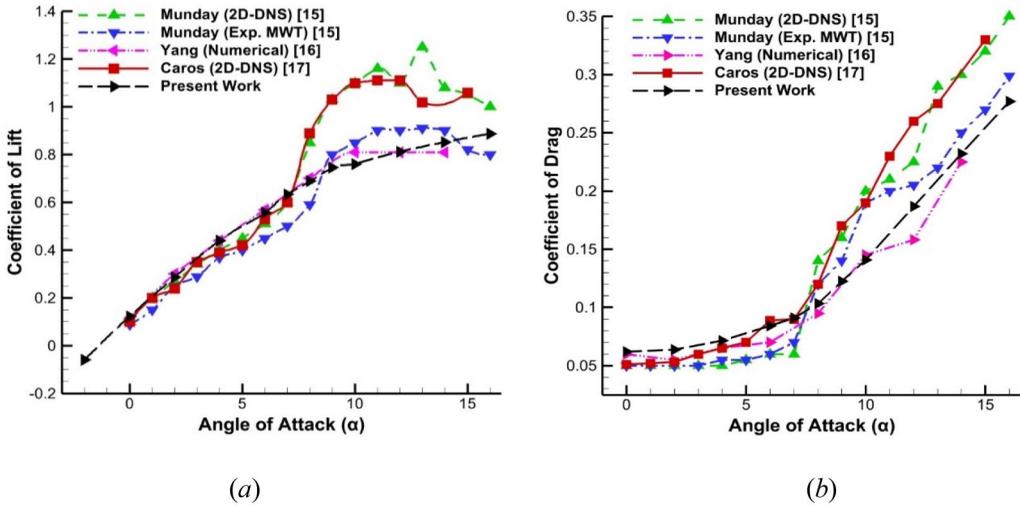
Figure 3. Validation for the coefficient of (a) lift and (b) drag at Re = 3,000 and Δh = 0.05C.

The Spalart-Almaras turbulence model has been used, and the comparison has been done with Munday [18], Yang [19], and Caros [17]. Munday [18] has done both DNS simulations and experimental analysis, whereas Caros [17] and Yang [19] have performed numerical simulations. The results from the current research agree with the previous literature, and the agreement is more with the experimental analysis. Since the existing numerical model is found to be giving results that agree with previous results, authors have used a similar turbulence model to analyze the aerodynamic characteristics of the triangular airfoil with the varying maximum height from 4% to 6% of chord length.

3. Results and discussion

Flow past a triangular airfoil for various Re. in Mars atmospheric conditions considering the different highest thicknesses of the airfoil (Δh). The simulations have been done for 11 angles of attack for each maximum height for the airfoil and five chord-based Re = 3,000, 4,000, 5,000, 6,000 and 7,000. For Mars, atmospheric conditions, the coefficients of force for varying Re. have demonstrated an increase in lift coefficient up to 16° angle of attack [9]. The lift curve however becomes less steep with an increase in α.

3.1. Force coefficients at various Δh

1. Δh = 0.04C: At lowest Δh, C_l increases with increasing Re. as shown in Figure 4. The curve demonstrates linearity up to $\alpha = 6°$ and becomes non-linear after that. This non-linear curve varies for various Re. At the lowest Re = 3,000, the curve is the most non-linear. The stall isn't achieved till $\alpha = 6°$, but the rate of increase decreases significantly after $\alpha = 8°$. From $\alpha = 6°$ to 12°, the non-linearity is most prevalent and the values are lowest at Re. 3,000. When the Re. is increased the values in this range increases significantly. But, the increased values show a higher increase when the Re. increased from 3,000 to 4,000. The coefficient of drag exhibits a progressive rise at lower angles of attack, with a marked escalation occurring post $\alpha = 6°$ across all Reynolds numbers. Particularly, at Re = 3,000, elevated drag coefficients are notable at lower angles of attack, though this pattern shifts at $\alpha = 16°$, where the peak drag is observed for Re. 5,000. This trend mirrors the behavior of the lift coefficient, which also reaches its zenith at Re. 5,000 and $\alpha = 16°$.
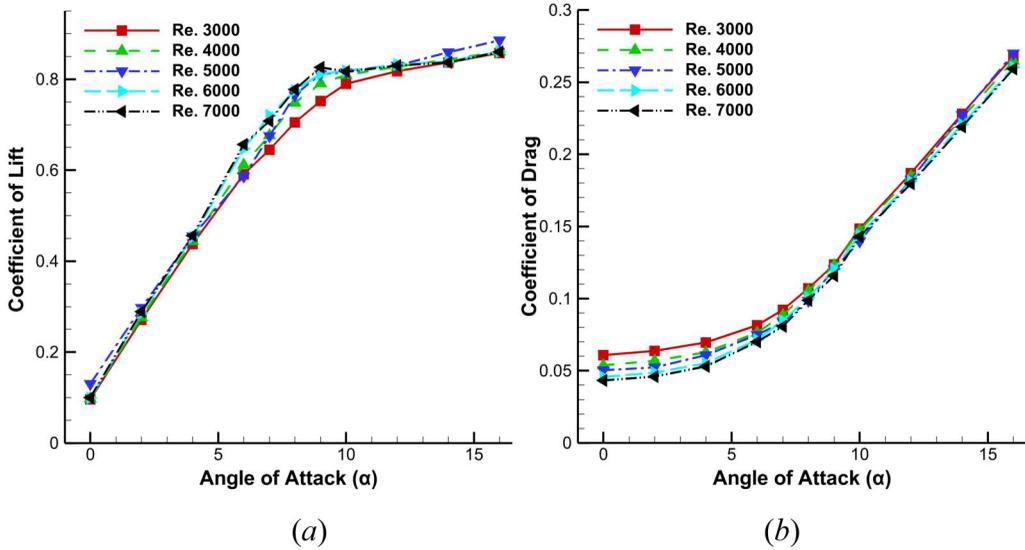
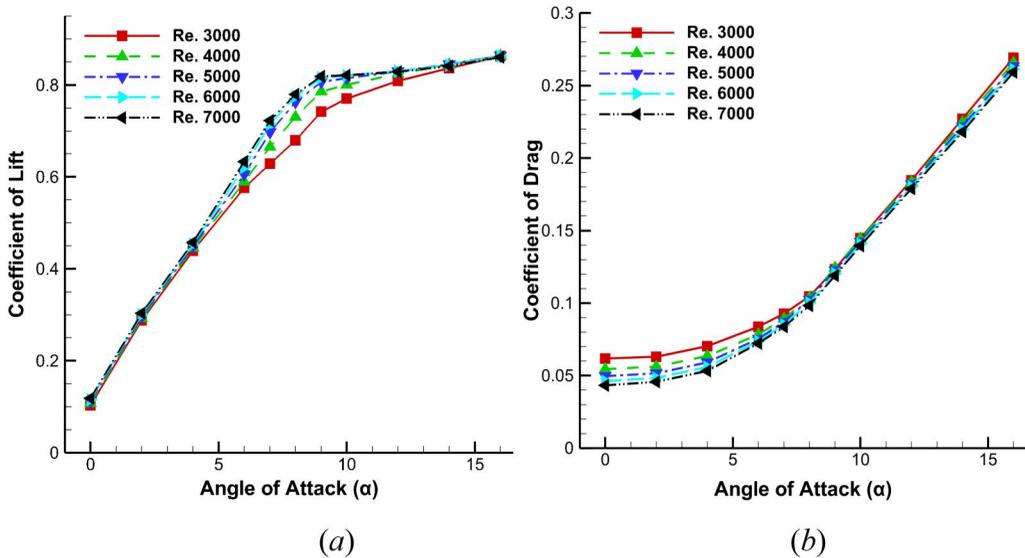**Figure 4.** Coefficient of (a) lift and (b) drag at various $\Delta h = 0.04C$.

Figure 5. Coefficient of (a)lift and (b)drag at various re. and $\Delta h = 0.45C$.

2. $\Delta h = 0.045C$: When the maximum thickness is increased to $\Delta h = 0.045C$, the non-linearity is the coefficient of lift lower than when $\Delta h = 0.04C$ in Figure 5. The curve is much smoother for all the Reynold numbers when compared to $\Delta h = 0.04C$ and much similar to $\Delta h = 0.05C$. The non-linear nature is much more prevalent at Re. 3,000 when compared to the higher Re. At Re = 4,000, the non-linear nature has changed to a large extent than $\Delta h = 0.05C$. The flattening of the curve happens but at a higher angle of attack but still has a decreased non-linear curve to a great extent. The drag coefficient for this Δh closely mirrors the trend observed at $\Delta h = 0.04C$. Notably, at $\alpha = 16°$, the highest drag coefficient is recorded for Re = 3,000, contrasting with $\Delta h = 0.04C$, where this peak occurred at Re = 5,000.
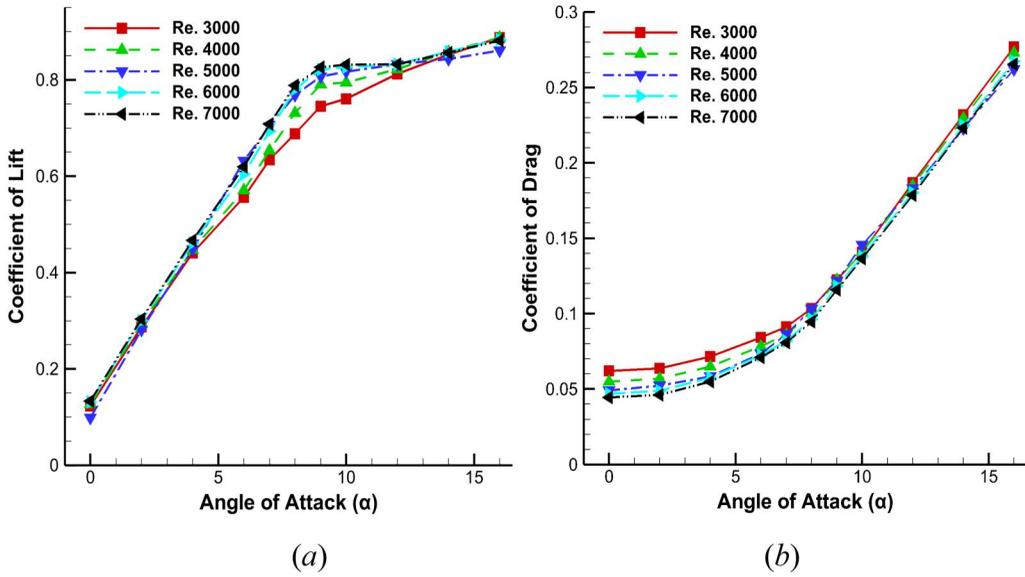
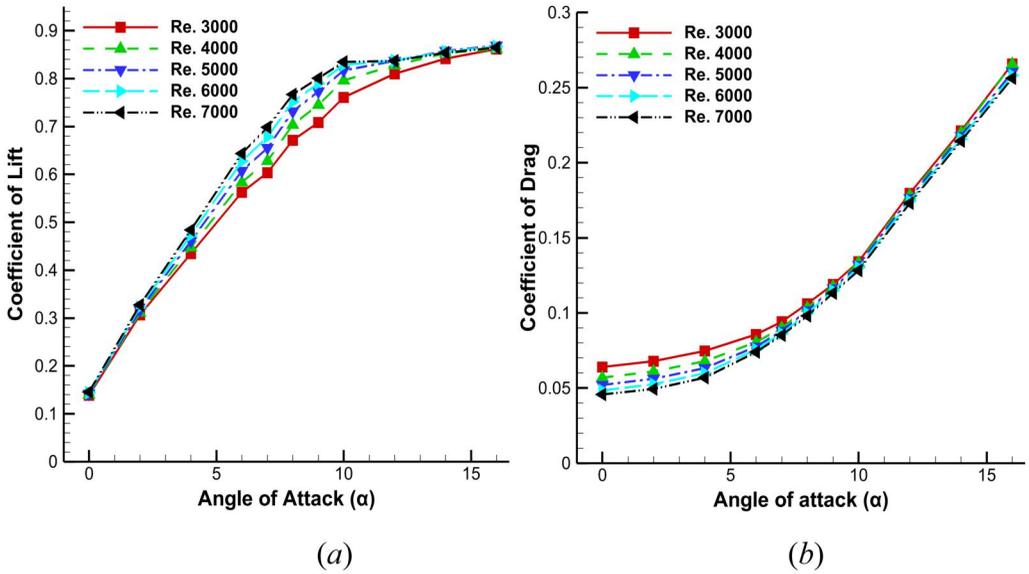**Figure 6.** Coefficient of (a)lift and (b)drag at various re. and Δh = 0.05C.

Figure 7. Coefficient of (a)lift and (b)drag at various re. and Δh = 0.06C.

3. Δh = 0.05C: When the Δh = 0.05C, C_l increased with the increasing Re. but at $\alpha = 16°$, the value decreases with increasing Re. in Figure 6. The coefficient of drag has decreased for all Re. The nonlinearity in lift coefficient has decreased with the increase in Re. and a significantly smoother curve has been obtained for Re = 5,000, 6,000, and 7,000. At these Re., the value has not followed the increment trend as followed by Re = 3,000, and 4,000. The curve flattens to a certain extent from $\alpha = 8°$ to $\alpha = 12°$. The value after $\alpha = 12°$ increases for all the investigated Re. In the range of angles of attack where the values have been non-linear, the increment has been higher for Reynolds number 4,000 to 7,000 and the highest increment has been from Reynolds number 3,000 to 4,000. The coefficient of drag has decreased

with the increasing Reynolds number and the trend seems to be similar for all the Re. When the Reynolds number is changed from 3,000 to 4,000, the highest decrement is recorded at lower angles of attack up to $\alpha = 6°$. The decrease after $\alpha = 6°$ is not much significant and the decrement decreases with the increasing Reynolds number. At $\alpha = 16°$, the drag coefficient is highest for Reynolds number 3,000. The lift coefficient curve never reaches a stall position up to $\alpha = 16°$. The stall could be reached after that or the aerodynamic performance of the airfoil would deteriorate. When the maximum thickness Δh of the airfoil is decreased to $\Delta h = 0.04$, the non-linearity decreases at Reynolds number 3,000 but increases at a higher Reynolds number. For Reynolds number 7,000, the non-linearity has started at $\alpha = 6°$ to $\alpha = 10°$.

4. $\Delta h = 0.06C$: At $\Delta h = 0.06C$, the lift slope becomes highly non-linear for all the Re. starting from $\alpha = 6°$ to $\alpha = 10°$ in Figure 7. The nature of the curve becomes highly non-linear but for nearly all the Re., the non-linearity is similar with exception of Re. 3,000. The nonlinearity is the lowest for Re = 7,000 as the curve shows a good linearity from $\alpha = 8°$. For Reynolds, number 3,000, the lift is significantly lower during the range of $\alpha = 6°$ to $\alpha = 10°$, where the non-linear is prevalent when compared to higher Re., although at $\alpha = 16°$, the difference decreases. The coefficient of drag decreases with the increase in Re. at this Δh. The decrease in the values tends to lower at higher angles of attack when compared with $\Delta h = 0.05C$, and at lower angles of attack, the decreases follow the same trend of $\Delta h = 0.05C$.

3.2. Force coefficients at various Reynolds number

1. Re = 3,000: At Re = 3,000, for $\alpha < 4°$, C_l is higher for $\Delta h = 0.06C$, followed by $\Delta h = 0.05C$, $\Delta h = 0.045C$, and $\Delta h = 0.04C$. Between $6° < \alpha < 12°$, due to the non-linearity, the highest value is for $\Delta h = 0.04C$ shown in Figure 8, followed by $\Delta h = 0.045C$, $\Delta h = 0.05C$ and $\Delta h = 0.06C$. For $\alpha > 12°$, the highest value is achieved by the airfoil having $\Delta h = 0.05C$, followed by 0.04C, 0.045C, and 0.06C. The coefficient of drag up to $\alpha < 8°$ increases with an increase in the Δh of the airfoil. The value higher than $\alpha > 9°$ to $\alpha < 12°$ shows a reverse trend, but at $\alpha = 12°$, the value is highest for $\Delta h = 0.05C$, followed by $\Delta h = 0.04C$, $\Delta h = 0.045C$, and $\Delta h = 0.06C$.
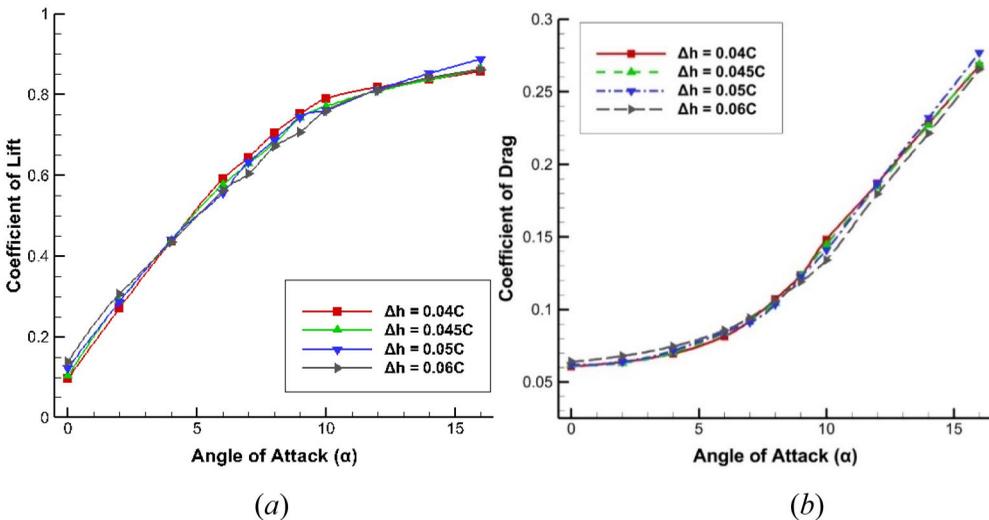

Figure 8. Coefficient of (a)lift and (b)drag at Re = 3,000.

2. Re = 4,000: At Re = 4,000, in Figure 9 below $\alpha < 4°$, the C_l increases with an increase in Δh, but from $\alpha = 6°$ to $\alpha = 10°$, the trend reverses. At $\alpha = 12°$, again, the C_l is highest for $\Delta h = 0.06C$ and followed by $\Delta h = 0.04C$, 0.045C, and 0.05C. But, at $\alpha = 14°$ and 14°, the highest C_l is reported at $\Delta h = 0.05C$ and lowest for $\Delta h = 0.04C$. The C_d up to $\alpha = 6°$ have shown an increase for $\Delta h = 0.06C$ and followed by $\Delta h = 0.05C$, 0.045C, and 0.04C. From $\alpha > 6°$ to $\alpha < 12°$, the non-linearity is prevalent as at $\alpha = 6°$, the highest C_d for $\Delta h = 0.06C$ is followed by $\Delta h = 0.05C$, 0.045C, and 0.04C. From $\alpha > 12°$ to $\alpha = 16°$, the highest drag is reported for $\Delta h = 0.05C$, which is followed by $\Delta h = 0.04C$, $\Delta h = 0.045C$, and $\Delta h = 0.06C$.

3. Re = 5,000: At Re = 5,000, the C_l is highest for $\Delta h = 0.06C$ shown in Figure 10, up to $\alpha < 6°$, and the non-linearity starts from $\alpha = 6°$, up to $\alpha < 12°$. The value increases after $\alpha = 12°$, for $\Delta h = 0.04C$ followed by $\Delta h = 0.06C$, $\Delta h = 0.045C$, and $\Delta h = 0.05C$. The C_d is
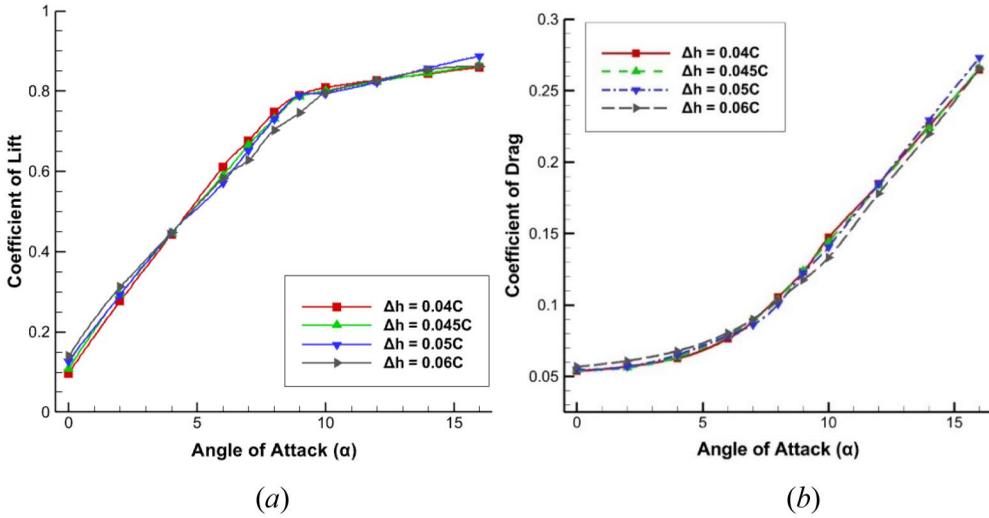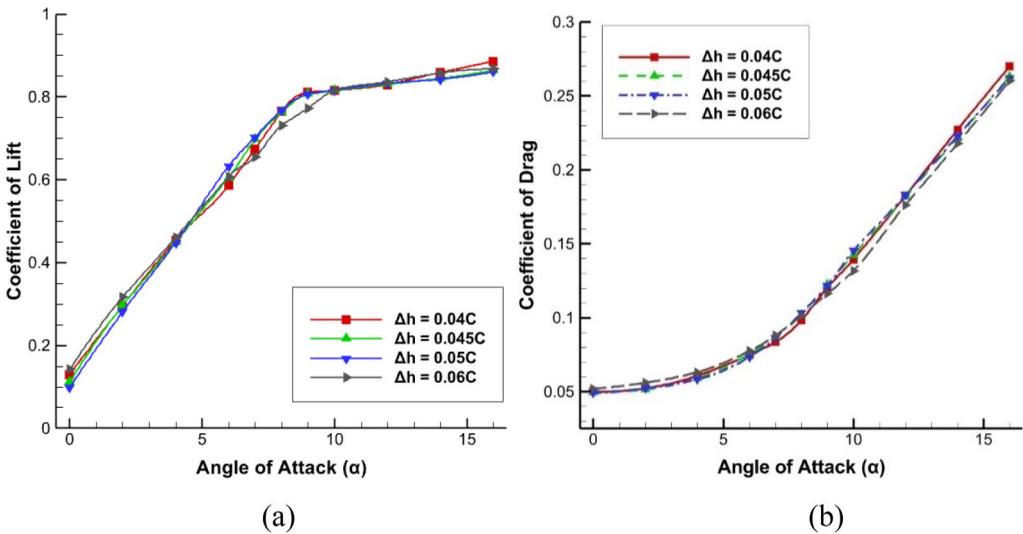

Figure 9. Coefficient of (a)lift and (b)rag at Re = 4,000.

Figure 10. Coefficient of lift and drag at Re = 5,000.

highest up to $\alpha = 7°$, for $\Delta h = 0.06C$, and becomes non-linear after that but the value from $\alpha = 9°$ to $\alpha = 16°$, is lowest.

4. $Re = 6,000$: At $Re = 6,000$, the C_l is highest for $\Delta h = 0.06C$ up to $\alpha < 6°$ same as for Re. 5,000. The value becomes non-linear as the α increases and is prevalent up to $\alpha = 12°$, after which $\Delta h = 0.05C$ has shown the highest C_l. C_d is highest for $\Delta h = 0.06C$ shown in Figure 11 up to $\alpha = 7°$, but decreases after that and remains lower for all the further angles of attack. For $\alpha > 12°$, the highest C_d has been reported for $\Delta h = 0.05C$.

5. $Re = 7,000$: When the Re. is increased to 7,000, for $\alpha > 4°$, the highest C_l has been achieved for airfoil at $\Delta h = 0.06C$ shown in Figure 12, which then decreases with increasing α. From $4° < \alpha < 12°$, the highest C_l is achieved for $\Delta h = 0.04C$ at $\alpha = 6°$, and it remains fluctuating. For $\alpha > 12°$, the highest C_l, has been achieved for $\Delta h = 0.05C$. For $\alpha > 9°$, Cd is highest for $\Delta h = 0.06C$ and the lowest value reaches $\Delta h = 0.05C$ for $\alpha > 9°$ with
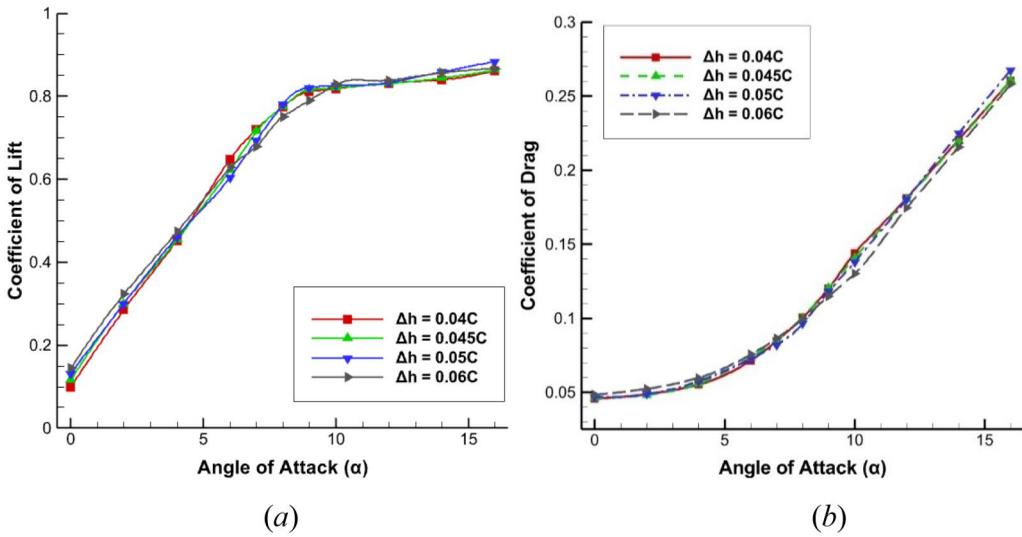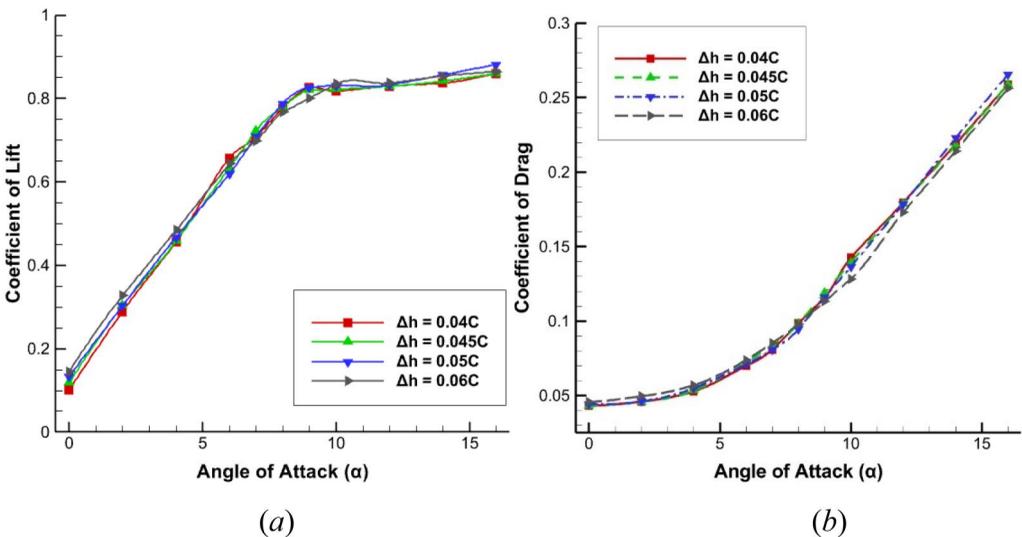

Figure 11. Coefficient of lift and drag at Re = 6,000.

Figure 12. Coefficient of lift and drag at re = 7,000.

exception of $\alpha > 7°$. When the $8° < \alpha < 14°$, the C_d is highest for thickness $\Delta h < 0.05C$, and is highest for $8° < \alpha \leq 16°$ at $\Delta h < 0.06C$.

The curve flattens after the non-linearity and for Reynolds number 7,000, the curve flattening is more prevalent than other Re. The coefficient of lift is observed to be higher for Reynolds number 5,000 when compared to others up to $\alpha = 4°$. The coefficient of drag for $\Delta h = 0.04C$ has shown a similar trend of decrease with increasing Re. as for $\Delta h = 0.05C$. The decrement is higher at lower angles of attack which decreases when the Re. increases. The coefficient of drag is lowest for Re = 7,000 for all the angles of attack and the value is higher at $\alpha = 16°$ for Re = 5,000 [9].

3.3. Pressure coefficients and pressure contours

Figures 13–15 illustrate the significant variation in pressure coefficient on the airfoil surface across different Reynolds numbers and angles of attack (α). The Cp distribution is presented for two thicknesses, Δh, at 0.04C and 0.06C, with curves selectively shown for angles of attack displaying nonlinear lift coefficients. The upper curve at angle α represents the pressure side, while lower curves depict the suction side. At $\alpha = 0°$, the upper curve, remaining relatively constant, represents the lower surface, whereas the lower curve reflects pressure values on the upper surface, decreasing to a minimum at the point of maximum thickness.

As angle of attack (α) increases, the phenomenon diminishes due to changes in the incoming fluid flow shape compared to $\alpha = 0°$, resulting in a decrease in pressure coefficient (Cp). At $\alpha = 6°$, around 0.2m of chord length, Cp is higher compared to increases at various α on the suction surface. Variation in Cp is less significant on the pressure surface of the airfoil, up to 0.7m of chord length. The increase in Cp at $\alpha = 12°$ is notably higher up to 0.2m of chord length for $\alpha < 12°$, leading to lower lift coefficients (Cl) at higher α, as depicted in Figure 4.

With increasing Re., this phenomenon can be seen in Figure 13–15 (a). The increase in C_p for $\alpha = 6°$, up to 0.3m of the chord length is also higher on the suction side when compared to the higher angles of attack, and with increasing Re., this increment decreases on the suction surface up to 0.3m. When $\Delta h = 0.045C$, the increased thickness results in lower C_p, value on the suction surface along the chord length up to 0.55m for $\alpha = 0$. C_p, increases up to 0.3m for $\alpha \geq 6°$, and shows higher difference when $\alpha = 6°$ is compared to $\alpha = 7°$ and higher angles of attack. This can be seen as a fluctuation for $\alpha = 6°$ in Figure 13–15(a, b) and the difference can also be
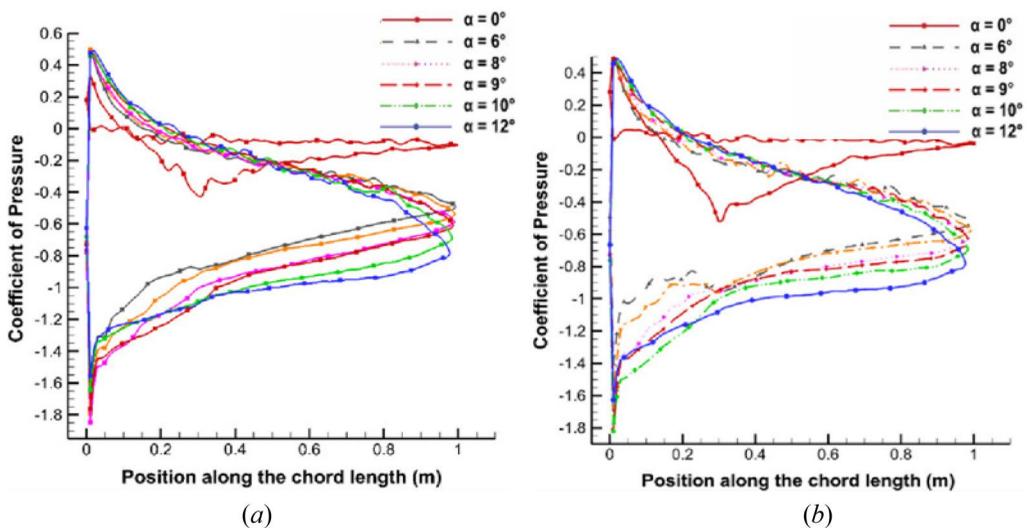

Figure 13. C_p Distribution on both airfoil surfaces at Re = 4,000, (a) $\Delta h = 0.04C$, (b) $\Delta h = 0.06C$.
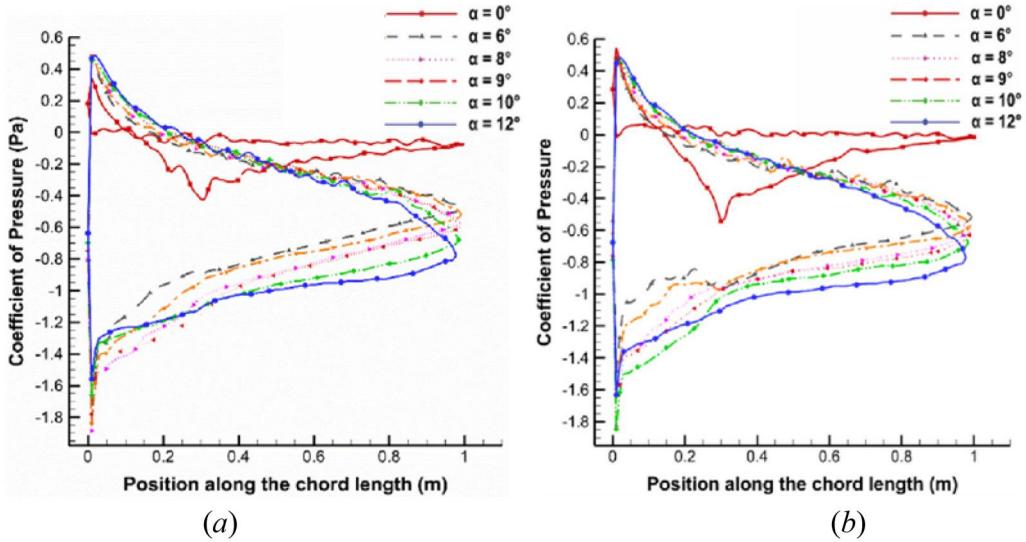
Figure 14. C_P Distribution on both airfoil surfaces at Re = 5,000, (a) $\Delta h = 0.04C$, (b) $\Delta h = 0.06C$.
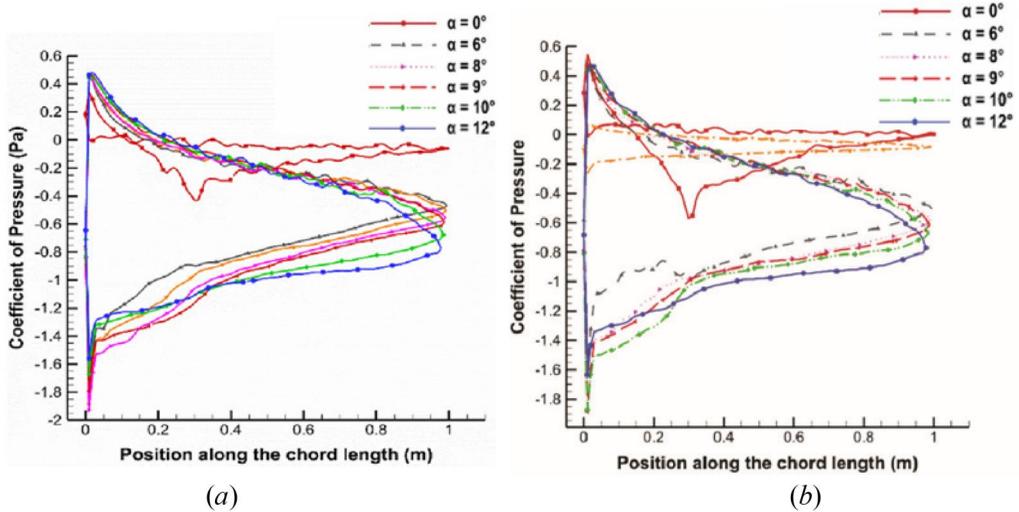

Figure 15. C_P Distribution on both airfoil surfaces at Re = 6,000, (a) $\Delta h = 0.04C$, (b) $\Delta h = 0.06C$.

visualized. C_p on the suction surface continues to increase up to 0.4m along the chord length for high α, most evident in the plot at $\alpha = 12°$ for increasing Re. The fluctuating C_p is a bit suppressed with increasing angles of the attack to a great extent and at higher α, the value increases up to 0.3m length along the axial direction. But a small decrease is also noticed at high Re. for $\alpha = 12°$ up to 0.3m. Fluctuations can also be seen on the suction surface at lower Re. and at low α, however it dissipates with the increasing Re. and at Re = 7,000, one significant decrease in C_p could be noticed. C_p fluctuations on the suction surface for $\Delta h = 0.05C$ is much less than the above two cases which shows a higher decrease in C_p along the chord length. The decrease becomes more evident with increasing Re. as the decrease shown in the Figure 13–15(a, b) demonstrates it by showing the lowest value and the curve becoming more steeper compared to the lower Re. The fluctuations for $\alpha \geq 6°$, shows an increase up to 0.4m, with a sudden drop at 0.3m along the chord length. Higher unsteadiness is found at up to 0.3m for most α, but at higher $\alpha = 12°$, C_p increases at 0.04m itself at a higher Re.
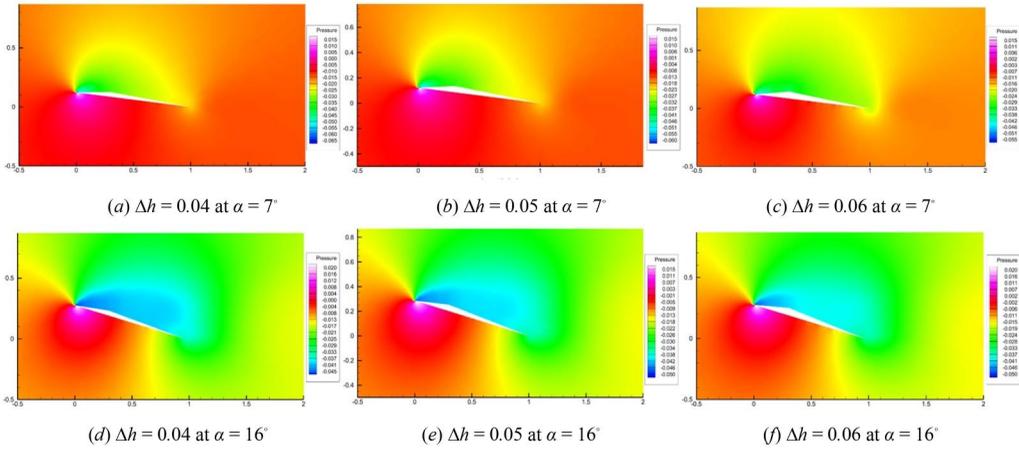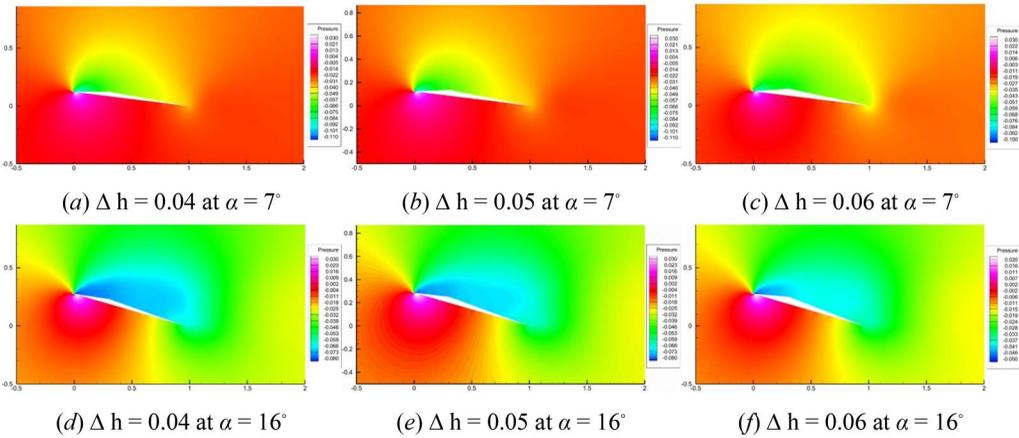
Figure 16. Pressure contours at Re = 3,000.

Figure 17. Pressure contours at re= 4,000.

Pressure on the pressure side is higher than the suction side, which in turn develops the lifting force. Figure 16–18 shows the pressure contours around the triangular airfoils at various Δh for three different Re. The pressure on the contours in Figure 16 (a) at $\alpha = 7°$ shows an increased pressure on the pressure surface, with the highest pressure being near the leading edge and decreasing along the chord length. The lowest pressure on the suction side is near leading edge and then it increases along the chord length. The pressure on the suction and pressure increases near the trailing edge. The pressure downstream is higher for Δh = 0.04C when compared to Δh = 0.05C, and 0.06C. A significantly higher pressure is generated on pressure surface at the trailing edge at Δh = 0.04C, which helps in generating higher lift. At higher Δh = 0.06, a lower pressure develops near the trailing edge on the pressure side, which decreases the lift force of the airfoil. The higher lift at Δh = 0.04 is also quite evident due to high-pressure contours on the pressure surface is up to 0.5C. When α is increased to 8°, the pressure on the pressure side decreases compared to low α near the trailing edge. At the highest Δh, the downstream pressure is the lowest.

Pressure on the airfoil's pressure side decreases with an increase in Δh, at Re = 4,000 as shown in Figure 17. When the Δh increases, the pressure decreases. On the pressure surface, the pressure along the chord length decreases and for the highest Δh, the pressure is lowest near the trailing edge at $\alpha = 7°$. On the suction side the pressure decreased as Δh is increased toward the
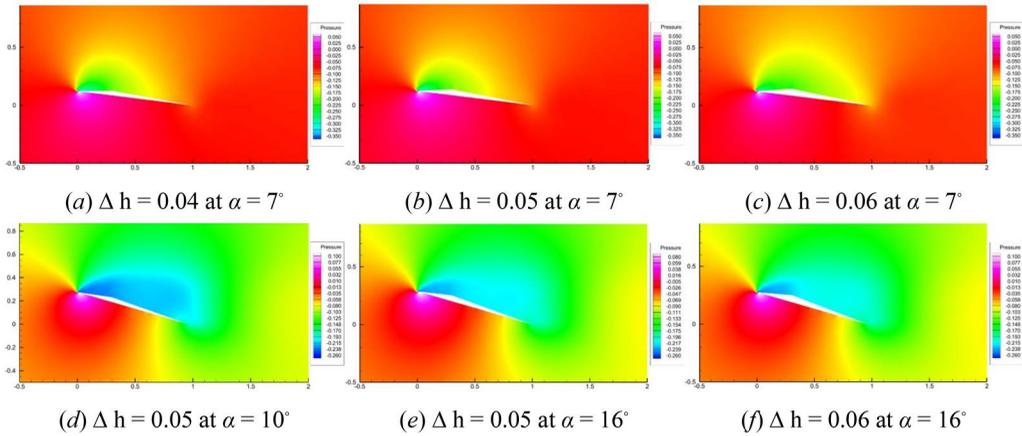
Figure 18. Pressure contours at re= 7,000.

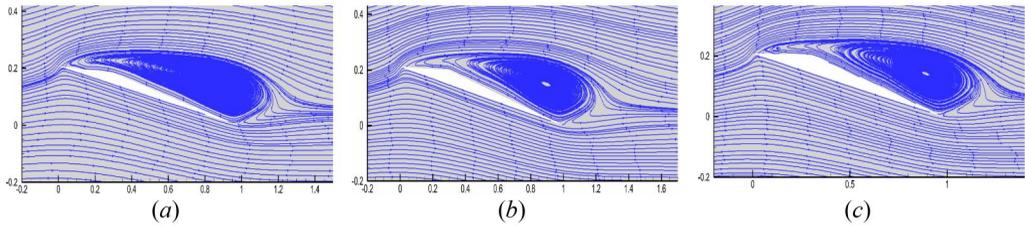(a) Δ h = 0.04 at α = 7°   (b) Δ h = 0.05 at α = 7°   (c) Δ h = 0.06 at α = 7°

(d) Δ h = 0.05 at α = 10°   (e) Δ h = 0.05 at α = 16°   (f) Δ h = 0.06 at α = 16°

(a)   (b)   (c)

Figure 19. Streamlines at Re = 3,000 at α= 12° with different (a) Δh = 0.04C, (b) Δh = 0.05C and (c) Δh = 0.06C.

trailing edge. When α is increased to $10°$ the pressure on the pressure surface is significantly increased for $\Delta h = 0.06C$, which in turn increases C_l and reaches the highest value followed by $\Delta h = 0.05C$ and $0.04C$. When α is further increased the pressure for various Δh changes abruptly resulting in unsteady airfoil performance. At the highest investigated α the contours on the pressure side become higher and a bit unstable near the trailing edge which is attributed to the higher C_l at $\Delta h = 0.05C$. At other Δh, the pressure contours are more stable comparatively which alters the airfoil performance at high α.

When the Re. increases the pressure on the pressure side changes randomly which can be evidenced by the pressure contours. At $\alpha = 7°$, for $\Delta h = 0.06C$ the pressure on the pressure side is lowest compared to other Δh as shown in Figure 18. When α is increased to $10°$, the pressure contours show the highest pressure for $\Delta h = 0.05C$ followed by $\Delta h = 0.06C$ which influences the force coefficients too. At the highest investigated α pressure at lowest Δh highest which leads to a higher lift coefficient followed by $\Delta h = 0.06C$. The downstream pressure becomes unstable because of high α.

3.4. Streamlines of airfoil

When $\Delta h = 0.04C$ at Re = 3,000 in fewer flow separation regions are generated which then increases near the leading edge as shown in Figure 19. At higher α, the flow separation increases but at this Δh, the vortices increase compared to higher Δh, and are decomposed generating a bigger flow circulation zone. When the Δh is highest, a vortex is generated near the leading edge at $\alpha = 12°$, which is not found at other Δh, which is the main result of the increased $\Delta h = 0.06C$. With increasing Δh, the downstream circulation region also increases, i.e. the higher Δh results in larger boundary layer separation and vortex generation.
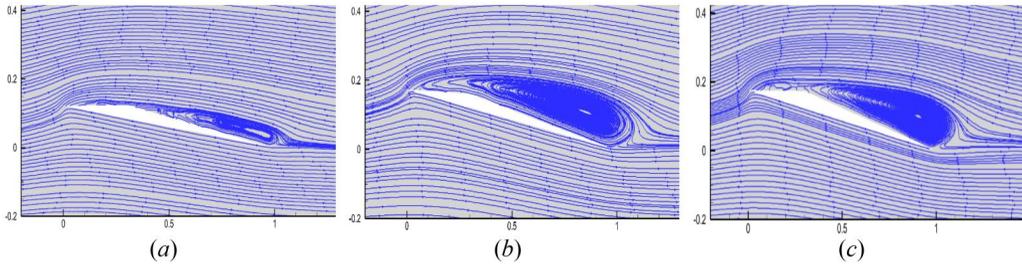
Figure 20. Streamlines at Re = 4,000 with different (a) $\Delta h = 0.04C$, $\alpha = 7°$, (b) $\Delta h = 0.04C$, $\alpha = 10°$, and (c) $\Delta h = 0.05C$, $\alpha = 10°$.
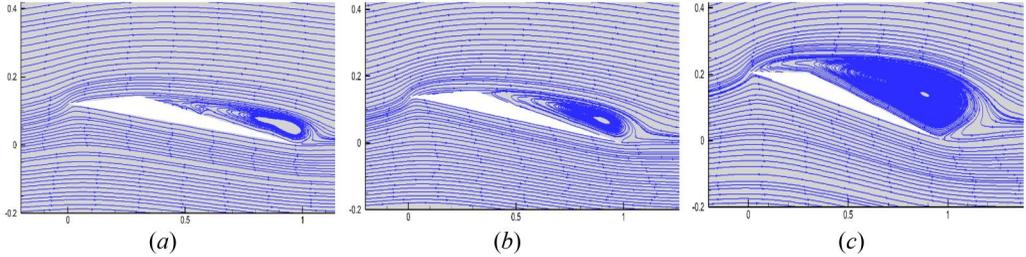

Figure 21. Streamlines at Re = 5,000 with $\Delta h = 0.06C$ at different $\alpha = $ (a)7°, (b)8° and (c)12°.

When the Re. increased to 4,000, vorticity on the suction side is found to be multiple at $\alpha = 7°$ as shown in Figure 20. With increase in α, the flow separation which was until near the trailing edge at 0.04C, a vortex appears near the leading edge. This vortex with increasing α gets mixed with the bigger vortex, thus generating a much bigger circulation region. At $\alpha = 10°$, flow separation increases and becomes completely unstable along the chord length before 0.3m for $\Delta h = 0.04C$ as shown in Figure 20. Two fully developed circulation zones, one bigger and another small, generated for $\Delta h = 0.05C$, between 0.6C to 0.7C and 0.7C to 1.05C.

At a higher Re., the flow separation on the suction surface near the leading edge is higher comparatively. The flow separation at Re = 5,000 for various Δh shows that the flow separation is less or negligible, sometimes no separation for higher Δh up to 0.3C along the chord length as shown in Figure 21. This phenomenon can be well asserted by $\alpha = 7°$ and 8°, for $\Delta h = 0.06C$, where no separation is visible. Flow before 0.3C along the chord length shows random flow separation without proper flow circulation region for low Δh. This flow separation at higher Δh generates into an appropriate region of circulation which degenerates into the bigger recirculation region generated near the trailing edge, finally generating into a more prominent recirculation region at higher α. Also, at higher Δh, the flow separation region near the leading edge before 0.3C along the chord length shows a bit decrease at higher α which is because of the increased maximum thickness of the airfoil, because this phenomenon decreases with decreasing Δh.

When the Re. is further increased to 6,000, the separation increases with increasing α as shown in Figure 22 and 23. When Δh is 0.04C, the flow separation before 0.3C along the chord line on the suction surface shows multiple small circulation regions which are relatively unstable, which then becomes one single circulation at $\Delta h = 0.045C$, and then the circulation is almost negligible at $\Delta h = 0.05C$ for $\alpha = 8°$. The flow becomes streamline at this place at the highest investigated Δh. At $\alpha = 9°$, the flow separation over the suction side is just one bigger recirculation region at lower Δh, which becomes smaller, generating multiple circulation zone with increasing Δh, and tends to become free streamline. The vortex in downstream is not generated at lower Δh, and continues to increase with increasing in maximum airfoil thickness. An additional recirculation zone is observed at $\alpha = 16°$. The flow separation. The non-linearity is mainly observed for α
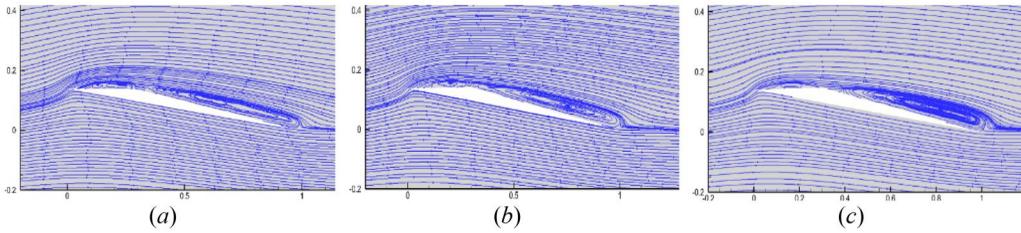
Figure 22. Streamlines at Re = 6,000 with $\alpha = 8°$ at different (a) $\Delta h = 0.04C$, (b) $\Delta h = 0.045C$ and (c) $\Delta h = 0.05C$.
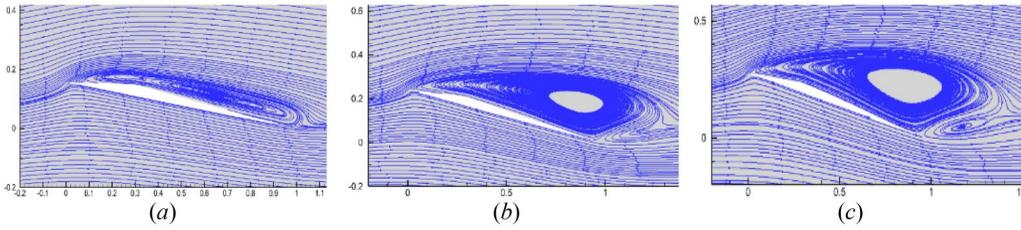

Figure 23. Streamlines at Re = 6,000 at different (a) $\Delta h = 0.04C$, $\alpha = 9°$,(b) $\Delta h = 0.04C$, $\alpha = 16°$ and (c) $\Delta h = 0.045C$, $\alpha = 16°$.
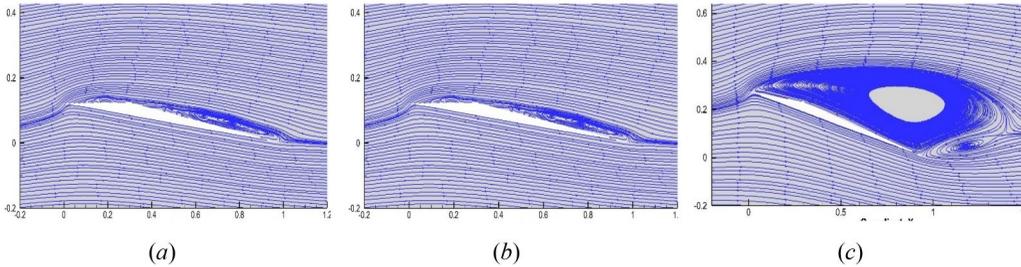

Figure 24. Streamlines at Re = 7,000 with $\Delta h = 0.04C$ for different angle $\alpha = $ (a) 7°, (b) 9° and (c) 16°.
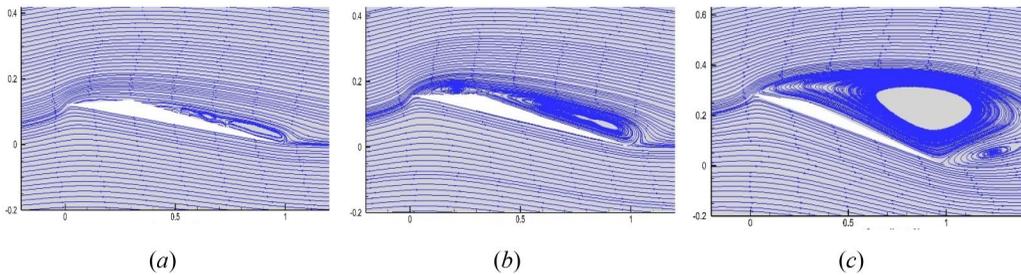

Figure 25. Streamlines at Re = 7,000 with $\Delta h = 0.05C$ for different angle $\alpha = $ (a) 7°, (b) 9° and (c) 16°.

where the flow separation on the suction surface starts to reach the apex of the airfoil. Multiple small flow instabilities forming vortices are found near these α.

Streamlines have been shown for Re = 7,000 at various Δh as shown in Figures 24–26. Flow separation occurs as α is increased. The flow circulation is initially generated at lower α near the trailing edge but with increasing α, the circulation region shifts toward the leading edge. When α is increased, as the flow starts getting separated near the leading edge too, small multiple vortices start forming which then decomposes generating a single large circulation region as the α is increased further. At the highest investigated $\alpha = 16°$, apart from a large vortex on the suction
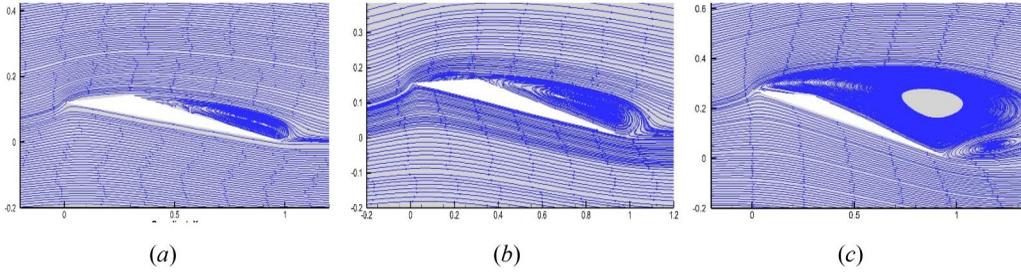
Figure 26. Streamlines at Re = 7,000 with $\Delta h = 0.06C$ for different angle $\alpha=$ (a) 7°, (b) 9° and (c) 16°.
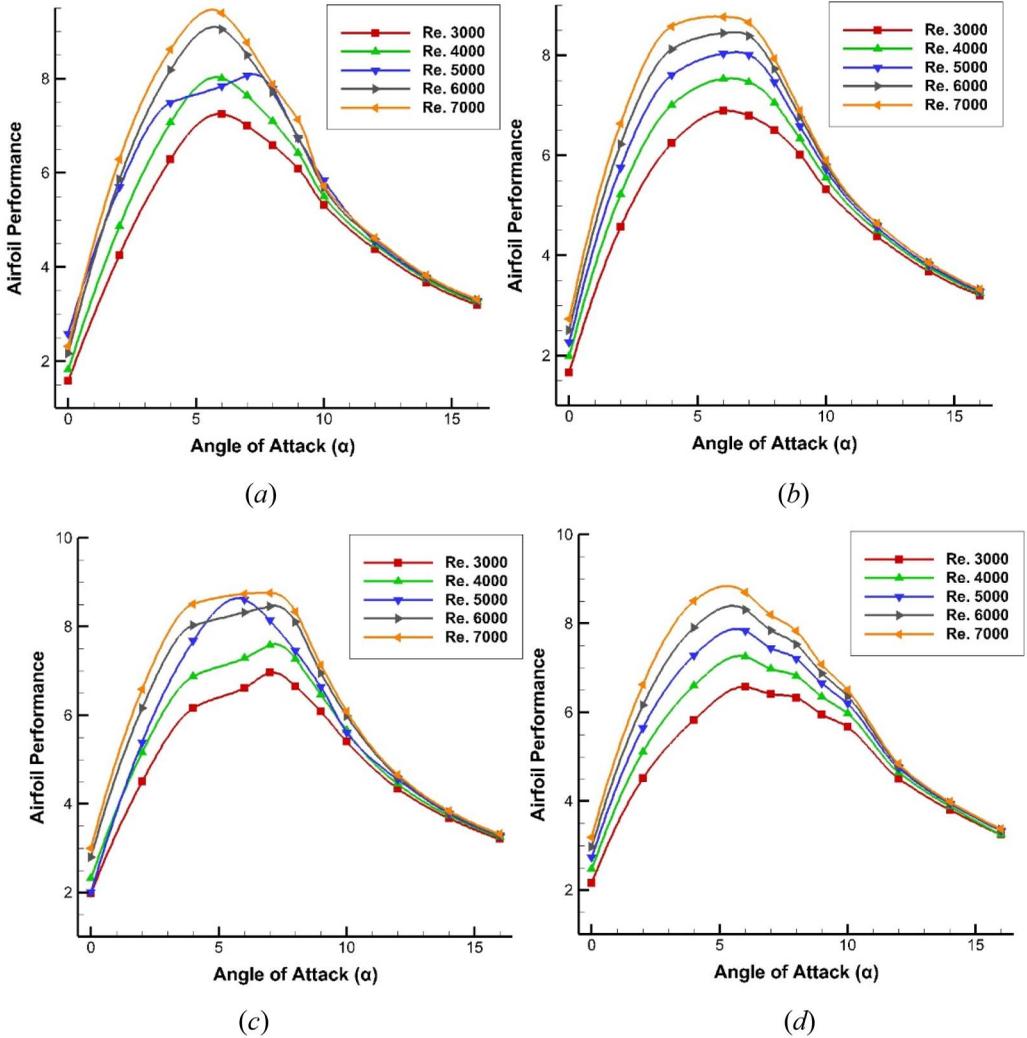

Figure 27. Aerodynamics performance at various re. for (a) $\Delta h = 0.04C$, (b) $\Delta h = 0.045C$, (c) $\Delta h = 0.05C$, and (d) $\Delta h = 0.06C$.

side of the airfoil, a resultant flow circulation happens downstream of the airfoil up to 0.4C downstream.

3.5. Airfoil performance

The lift-to-drag (L/D) ratio of the triangular airfoil at various angles of attack and Reynolds numbers, for various maximum thicknesses, has been reported in Figure 27. Hereafter, this metric will be referred to as airfoil performance. At low Re., the highest airfoil performance is at $\alpha = 6°$ for all Re. The highest value reaches Re = 6,000 and 7,000, at $\Delta h = 0.04C$ over 9°. From $\alpha = 12°$, the performance values do not change much for the $\Delta h = 0.04C$ and Low Re. From $\alpha = 4°$ to 8°, the performance has shown higher values compared to other α. The aerodynamic performance for $\Delta h = 0.04C$ is highest at $\alpha = 6°$ and then decreases. For $\Delta h = 0.05C$, the performance increases from $\alpha = 7°$ to 9°, after which the maximum Δh takes precedence. For the maximum Δh at $\alpha = 4°$ to 8°, the performance is lowest but increases after $\alpha = 9°$. So, for this Δh except for $\alpha = 6°$ to 9°, the values are highest.

4. Conclusions

Over the past decade, research into Martian aerodynamics has become increasingly crucial as humanity explores the possibility of living on Mars. However, understanding aerodynamics on Mars poses unique challenges due to significant atmospheric differences from Earth. While triangular airfoils have been extensively studied in aerodynamic research, fixed values for airfoil geometry have predominated, with limited exploration of variable values on a large scale.

In this study, we aim to investigate the aerodynamics of triangular airfoils at various chord-based Reynolds numbers ranging from 3,000 to 7,000. We employ a two-dimensional simulation approach using a URANS-based finite volume solver, with the Spalart-Allmaras turbulence model utilized for calculations. The benchmark airfoil considered in our analysis has a maximum thickness of 0.05 chord lengths and is located at 0.3 chord lengths from the leading edge. This research seeks to enhance our understanding of Martian aerodynamics and inform future design considerations for airfoils in extraterrestrial environments.

The lift coefficient at low Re. increases with increasing α and becomes non-linear after 6° up to 12°. The drag coefficient at lower α is low, and the curve becomes steep after about 8°. The non-linearity also varies for different Re. and Δh. At low Re., the lift coefficient for $\Delta h = 0.04C$ is found to be the least non-linear compared to other Δh. The curves fluctuate highly between $\alpha = 6°$ upto 12°. The aerodynamic performance of the airfoil at $\Delta h = 0.04C$, 0.045, 0.05, and 0.06 shows the highest value at $\alpha = 6°$, $\alpha = 5°$ to 7°, $\alpha = 6°$ to 7° and $\alpha = 5°$ to 6° respectively. The flow separation happens with increasing α, but results in the formation of a separation bubble at higher α. An additional flow recirculation zone is also observed at extremely high angles of attack. The additional zone is observed from $\alpha = 16°$, at Re = 7,000.

5. Future work

In future research, there is a need for a more thorough investigation into the effects of leading and trailing edges on airfoil performance. Direct Numerical Simulation (DNS) should be employed to comprehensively understand the flow behavior and nonlinearities. While the current study has provided insights into boundary layer separation, further analysis is required to explore additional recirculation zones using advanced flow measurement techniques. Additionally, a detailed examination of flow separation from the apex would contribute to a deeper understanding of airfoil behavior.

Moving forward with airfoil design, it is crucial to initiate the process with a meticulous examination of existing triangular airfoils. This involves refining the vertex and closely monitoring changes in the flow recirculation zone to extract valuable insights. Subsequent optimizations aimed at minimizing this recirculation zone hold promise for enhancing aerodynamic

performance. Furthermore, conducting detailed high-fidelity simulations would offer enhanced comprehension of fundamental flow phenomena in the Martian atmosphere, thereby guiding informed design decisions.

Disclosure statement

No potential conflict of interest was reported by the author(s).

Funding

ORCID

Wen-Chung Wu http://orcid.org/0009-0001-8080-816X
Ankit Kumar http://orcid.org/0000-0002-3177-5816

References

[1] L. Jiang, *et al.*, "Numerical study on aerodynamic performance of Mars parachute models with geometric porosities," *Space Sci. Technol.*, vol. 2022, pp. 1-13, 2022. DOI: 10.34133/2022/9851982.
[2] H. Zhao, Z. Ding, G. Leng and J. Li, "Flight dynamics modeling and analysis for a Mars helicopter," *Chinese J. Aeronautics, Chinese Society Aeronautics Astronautics Beihang Univ*, vol. 36, no. 9, pp. 221–230, 2023. DOI: 10.1016/j.cja.2023.05.007.
[3] E. Hébrard, *et al.*, "An aerodynamic roughness length map derived from extended Martian rock abundance data," *J. Geophys. Res*, vol. 117, no. E4, pp. 1-26, 2012. DOI: 10.1029/2011JE003942.
[4] J. N. Moss, R. C. Blanchard, R. G. Wilmoth and R. D. Braun, *Mars Pathfinder Rarefied Aerodynamics: Computations and Measurements," Technical Report*. NASA Langley Technical Report Server, pp. 1-17, 1998,
[5] K. T. Ediquist, P. N. Desai and M. Schoenenberger, "Aerodynamics for the Mars Phoenix entry capsule," *J. Spacecraft Rockets*, vol. 48, no. 5, pp. 1522-1529, 2011. DOI: 10.2514/1.46219.
[6] J. Balaram, *et al.*, "Mars helicopter technology demonstrator," AIAA SciTech Forum, . AIAA Atmospheric Flight Mechanics Conf., Kissimmee, Florida, USA, Jan, 2018. DOI: 10.2514/6.2018-0023.
[7] W. J. F. Koning, W. Johnson and B. G. Allan, "Generation of Mars helicopter rotor model for comprehensive analyses," *AHS Specialists' Conf. Aeromechanics Design Transformative Vertical Flight*, San Francisco, California, USA,2018,
[8] A. Kumar and A. B. Harichandan, "Generation of shock waves on an airfoil in Mars atmosphere," *6th Nat. SY ∼ P. Shock Waves*,. 2020.
[9] A. Kumar, "Numerical investigation of triangular airfoil in Martian atmosphere at low and high Reynolds number," Master thesis, Dept, Aeronautical Engineering, National Formosa Univ, 2023., Yunlin, Taiwan,
[10] P. R. Spalart and S. R. Allmaras, "A one-equation turbulence model for aerodynamic flows," *La Recherche Aerospatiale*, 30th Aerospace Sciences Meeting and Exhibit, Aerospace Sciences Meetings, AIAA-92-0439, pp. 5–21, 1992.
[11] F. Ning and L. Xu, "Numerical investigation of transonic compressor rotor flow using an implicit 3d flow solver with one-equation Spalart-Allmaras turbulence model," Proc. - Turbo Expo: Power Land, Sea, Air, ASME, 2014. DOI: 10.1115/2001-GT-0359.
[12] Y. Liu, P. Li and K. Jiang, "Comparative assessment of transitional turbulence models for airfoil aerodynamics in the low Reynolds number range," *J. Wind Engineering Ind. Aerodynamics*, vol. 217, pp. 104726, 2021. DOI: 10.1016/j.jweia.2021.104726.
[13] ANSYS Fluent., "Transport equation for the Spalart-Allmaras model." [Online], Available: https://www.afs.enea.it/project/neptunius/docs/fluent/html/ug/node412.htm
[14] P. Tabeling, *Introduction to Microfluidics*, Oxford, England: Oxford Univ. Press, 2005, pp. 37.
[15] Wikipedia., [Online], Available: https://en.wikipedia.org/wiki/Knudsen_number.
[16] H. K. Versteeg and W. Malalasekera, *An Introduction to Computational Fluid Dynamics: The Finite Volume Method*, 2nd ed. New York, NY: Pearson Education Limited, 2007.

[17]   L. Caros, *et al.*, "Direct numerical simulation of flow over a triangular airfoil under Martian conditions," *AIAA J*, vol. 60, no. 7, pp. 3961–3972, 2022. DOI: 10.2514/1.J061454.

[18]   P. Munday, K. Taira, T. Suwa, D. Numata and K. Asai, "Non-linear lift on a triangular airfoil in low-Reynolds-number compressible flow," *J. Aircraft*, vol. 52, no. 3, pp. 924–931, 2015. May. DOI: 10.2514/1.C032983.

[19]   H. Yang and R. Agarwal, "CFD simulations of a triangular airfoil for martian atmosphere in low-Reynolds number compressible flow," AIAA Aviation Forum, AIAA Paper 2019-2923, Jun, 2019. DOI: 10.2514/6.2019-2923.